Journal of
Astronomical Telescopes,
Instruments, and Systems

AstronomicalTelescopes.SPIEDigitalLibrary.org

Impact of crosshatch patterns in H2RGs on high-precision radial velocity measurements: exploration of measurement and mitigation paths with the Habitable-Zone Planet Finder

Joe P. Ninan
Suvrath Mahadevan
Gudmundur Stefansson
Chad Bender
Arpita Roy
Kyle F. Kaplan
Connor Fredrick
Andrew J. Metcalf
Andrew Monson
Ryan Terrien
Lawrence W. Ramsey
Scott A. Diddams

Joe P. Ninan, Suvrath Mahadevan, Gudmundur Stefansson, Chad Bender, Arpita Roy, Kyle F. Kaplan, Connor Fredrick, Andrew J. Metcalf, Andrew Monson, Ryan Terrien, Lawrence W. Ramsey, Scott A. Diddams, "Impact of crosshatch patterns in H2RGs on high-precision radial velocity measurements: exploration of measurement and mitigation paths with the Habitable-Zone Planet Finder," *J. Astron. Telesc. Instrum. Syst.* **5**(4), 041511 (2019), doi: 10.1117/1.JATIS.5.4.041511.

Downloaded From: https://www.spiedigitallibrary.org/journals/Journal-of-Astronomical-Telescopes,-Instruments,-and-Systems on 29 Oct 2019
Terms of Use: https://www.spiedigitallibrary.org/terms-of-use

Impact of crosshatch patterns in H2RGs on high-precision radial velocity measurements: exploration of measurement and mitigation paths with the Habitable-Zone Planet Finder

Joe P. Ninan,[a,b,*] Suvrath Mahadevan,[a,b] Gudmundur Stefansson,[a,b] Chad Bender,[c] Arpita Roy,[d] Kyle F. Kaplan,[c] Connor Fredrick,[e,f] Andrew J. Metcalf,[e,g] Andrew Monson,[a,b] Ryan Terrien,[h] Lawrence W. Ramsey,[a,b] and Scott A. Diddams[e,f]

[a]Pennsylvania State University, Department of Astronomy and Astrophysics, University Park, Pennsylvania, United States
[b]Pennsylvania State University, Center for Exoplanets and Habitable Worlds, University Park, Pennsylvania, United States
[c]The University of Arizona, Department of Astronomy and Steward Observatory, Tucson, Arizona, United States
[d]California Institute of Technology, Department of Astronomy, Pasadena, California, United States
[e]National Institute of Standards and Technology, Time and Frequency Division, Boulder, Colorado, United States
[f]University of Colorado, Department of Physics, Boulder, Colorado, United States
[g]Air Force Research Laboratory, Space Vehicles Directorate, Kirtland Air Force Base, New Mexico, United States
[h]Carleton College, Department of Physics and Astronomy, Northfield, Minnesota, United States

Abstract. Teledyne's H2RG detector images suffer from crosshatch like patterns, which arise from subpixel quantum efficiency (QE) variation. We present our measurements of this subpixel QE variation in the Habitable-Zone Planet Finder's H2RG detector. We present a simple model to estimate the impact of subpixel QE variations on the radial velocity and how a first-order correction can be implemented to correct for the artifact in the spectrum. We also present how the HPF's future upgraded laser frequency comb will enable us to implement this correction. © *2019 Society of Photo-Optical Instrumentation Engineers (SPIE)* [DOI: 10.1117/1.JATIS.5.4.041511]

Keywords: HxRG; crosshatch; precision radial velocity; near-infrared; detectors.

Paper 19038SS received Apr. 10, 2019; accepted for publication Oct. 8, 2019; published online Oct. 26, 2019.

1 Introduction

The Habitable-Zone Planet Finder (HPF) is a stabilized fiber-fed near-infrared (NIR) (0.81 to 1.28 μm) ultrastable precision radial velocity (RV) spectrometer commissioned on the 10-m Hobby–Eberly telescope (HET) at McDonald Observatory, with the scientific goal of discovering and confirming low-mass planets around M dwarf stars. HPF uses a 1.7-μm cutoff H2RG array (Hawaii-2RG HgCdTe 2048×2048) cooled to 120 K as the detector.[1] We have demonstrated intrinsic calibration precision as low as 6 cm/s and the measurement of differential stellar RVs at the 1.53-m/s level over months-long time scales, which is unprecedented in the NIR wavelength region.[2] Nevertheless, there are still avenues for improvement in the precision of NIR RVs.

NIR HxRG detectors suffer from various artifacts compared to optical CCDs, which need to be corrected for precision spectroscopic measurements. One of the artifacts that affects the subpixel quantum efficiency (QE) of pixels in HxRG are the subpixel crosshatch patterns. These are believed to be intrapixel QE variations due to lattice defects in the HgCdTe crystal layer.[3–5] (A recent talk by James Beletic at EPRV-VI conference showed these are due to surface corrugation developed at the misfit dislocations between the strained HgCdTe layer and substrate. Future Teledyne detectors might not have this issue.) On the detector flat images, these defects appear as long streaks of low QE pixels (see Fig. 1 for an example in HPF). Little work exists on measuring the dimensions of these structures and their impact on RV measurements under the traditional flat correction scheme. In Sec. 2, first we present a method to estimate the characteristic width, angle, and the QE inside the defect from 2-D flat images. In Sec. 3, we present our simple step model to study the impact of a subpixel QE defect on the spectrum. We also derive a simple model to quantify the impact on the RV estimate as a function of the model parameters and the density of crosshatch in H2RG. Based on these models, we present our proposed correction algorithm in Sec. 4 and how an upgraded HPF's laser frequency comb (LFC) will enable us to estimate the required coefficients for the proposed correction algorithm. We conclude this paper in Sec. 5.

2 Measuring Intrapixel Structure from the Flat Image

A uniformly illuminated flat image can be used to estimate the typical width, angle, and subpixel QE of the defects in the pixels. Figure 1(a) shows a small region of the HPF H2RG detector after high-pass filtering of a smoothly illuminated flat data. Ideally, we should also divide out the e^-/adu gain of each pixel to make a cleaner effective QE map of pixels. The angle of the crosshatch pattern can be measured precisely from the 2-D power spectrum of this image [Fig. 1(b)]. The angle was measured to be 14.8 deg for HPF's detector. The power in this 2-D Fourier power spectrum at the Nyquist frequency also shows the intrapixel structures are indeed under-sampled as expected by the pixel grid.

*Address all correspondence to Joe P. Ninan, E-mail: jpn23@psu.edu

2329-4124/2019/$28.00 © 2019 SPIE

Downloaded From: https://www.spiedigitallibrary.org/journals/Journal-of-Astronomical-Telescopes,-Instruments,-and-Systems on 29 Oct 2019
Terms of Use: https://www.spiedigitallibrary.org/terms-of-use

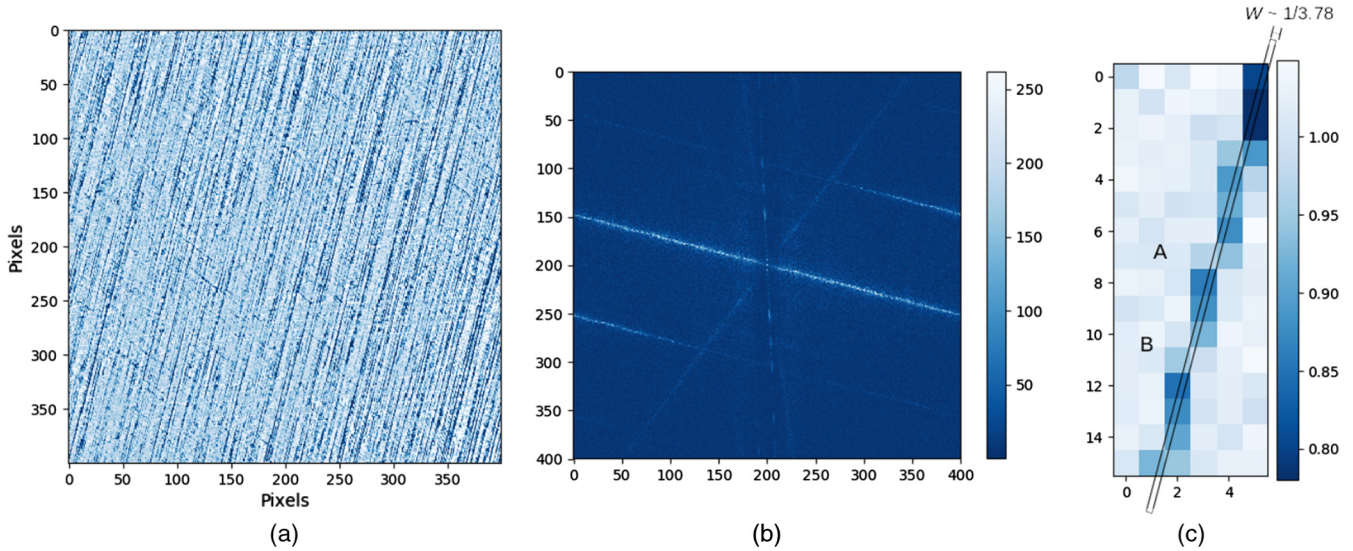

Fig. 1 (a) A sample crosshatch pattern region in HPF. (b) 2-D Fourier power spectrum of the region showing the angle of the crosshatches, as well as the power extending all the way to Nyquist sampling hinting the substructure nature of crosshatches. (c) Zoomed image of a typical 14.8-deg crosshatch QE variation pattern. Labels A and B mark two column crossover points of the subpixel crosshatch defect. A best fitted rectangular subpixel crosshatch with a width of 1/3.78 pixels is also overlayed on the pixels.

2.1 *Defect's Width w and QE q_d*

Figure 1(c) shows a zoomed image of a typical 14.8-deg crosshatch QE variation pattern in the HPF detector. The defect moves 3.8 rows before it jumps to the next column pixel.

To aid the discussion, two points of column crossovers are labeled as A and B in Fig. 1(c). Between A and B, the defect is fully contained inside a pixel boundary, and the pixel averaged relative QE of the middle three pixels (with respect to the outside region) is ~88%, i.e., a net QE drop of ~12%. The region labeled A has the defect moving from column 3 to 4 within a single row. The sum of the QE drop in both those crossover pixels combined is ~11%. In the region labeled as B, the defect is moving from column 2 to 3 across two rows. The sum of the QE drop in the crossover pixels combined is ~10% for both the rows. Hence, at least in this small patch of the crosshatch, the variation in q_d is small.

If the width of the defect is very narrow, at 14.8-deg angle, crosshatch will always take less than one pixel row to crossover. If the width is large, it will take multiple rows to crossover columns. Thus the shortest and longest crossover length scale (in units of rows) from one column to adjacent column constrains the width of the defect. Based on the 1 and 2 rows crossover width, we can estimate the width of the crosshatch defect (w) to be ~1/3.78 of a pixel, i.e., ~5 μm in Fig. 1(c). This geometrically constrained width of the defect is shown by the overlay.

Substituting $w = 1/3.78$ in the formula for average 88% QE (when the defect is fully inside a pixel) from Sec. 3; $[wq_d + (1-w)q] = 0.88q$, we obtain $q_d/q \sim 0.55$, i.e., the QE inside the defect of ~5 μm width is ~55% of the region outside the defect.

2.2 *Caveats of this Method*

The QE (q_d) inside the defect varies across the defect as one can see from the flat images [Fig. 1(a)]. So, q_d is not a single number and the value derived in the previous section is just a typical value in HPF's H2RG detector. The absolute gain differences of each neighboring pixel's amplifier limits the accuracy of this QE variation analysis. Hence, we have to make an accurate pixel-by-pixel e^-/adu gain map using individual pixel's photon transfer curve and then divide that out from the flat image shown here to improve the analysis. Finally, the relative neighboring pixel QE analysis outlined here is difficult in the regions with high density of crosshatch patterns.

3 Impact on Precision RV

3.1 *Modeling of Intrapixel QE Variation Due to Crosshatch Pattern in H2RG*

Consider the cross section of a pixel with a QE defect shown in Fig. 2. Let q be the QE outside the defect, and q_d be the QE inside the defect, which has a width w. Let x be the fractional position inside the pixel where the defect starts.

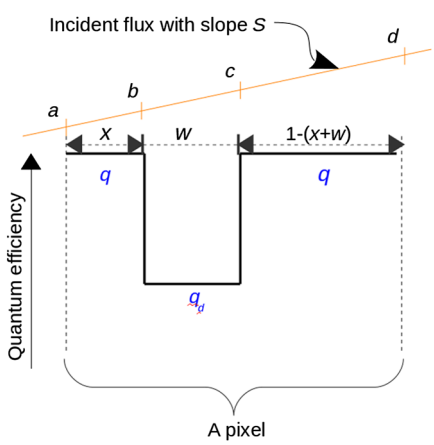

Fig. 2 Our simple 1-D step function model of intrapixel QE difference due to a crosshatch in the pixel. The width of the defect is w, and the QE inside and outside the defect is q_d and q, respectively.

Downloaded From: https://www.spiedigitallibrary.org/journals/Journal-of-Astronomical-Telescopes,-Instruments,-and-Systems on 29 Oct 2019
Terms of Use: https://www.spiedigitallibrary.org/terms-of-use

3.2 *Average Gain Correction Using Flat Illumination*

The average pixel gain is traditionally corrected by first illuminating the detector with a flat light source. The pixel to pixel relative gain factor is obtained from the measured deviation in pixel counts from neighboring pixels. Let C_{flat} be the counts we would have obtained from a pixel with no defect. In our defective pixel model, the measured count is given by $C_{\text{flat measured}} = C_{\text{flat}}[wq_d + (1-w)q]$. Hence, the standard flat correction recipe to convert measured counts to average pixel gain corrected count is to divide by $[wq_d + (1-w)q]$, i.e., $C_{\text{flat}} = \frac{C_{\text{flat measured}}}{[wq_d+(1-w)q]}$.

3.3 *Uncorrected Counts Due to Nonflat Illumination*

The average QE correction of a pixel, which has intrapixel QE variation, via flat-fielding process explained in the previous section is not valid when that pixel is illuminated by a nonflat illumination source. This will lead to an over-correction or under-correction by the flat-fielding process. For modeling this error term, consider an illuminating light source with slope S in pixel coordinates as shown in Fig. 2. Let a, b, c, and d be the incident flux values at 0, x, $x+w$, and 1 positions inside the pixel. Let C_s be the net counts from the pixel we would have obtained after flat correction if there were no defects in the pixel, i.e., $C_s = \frac{a+d}{2} \times 1$. Since S is the slope of the spectrum inside the pixel, we can parametrise $a = C_s - S/2$, $d = C_s + S/2$, $b = a + xS$, and $c = a + (x+w)S$. The measured counts in the defective pixel before flat correction is given by $C_{\text{s measured}} = \frac{a+b}{2}qx + \frac{b+c}{2}q_d w + \frac{c+d}{2}q[1-(x+w)]$. Substituting a, b, c, and d, and simplifying, we obtain $C_{\text{s measured}} = C_s[wq_d + (1-w)q] + Sw(q-q_d)(\frac{1-w}{2} - x)$. The average flat correction by dividing $[wq_d + (1-w)q]$ outlined in the previous section yields the flat corrected count as

$$C_{\text{s measured flat corrected}} = C_s + \frac{Sw(q-q_d)\left(\frac{1-w}{2} - x\right)}{[wq_d + (1-w)q]}. \tag{1}$$

Equation (1) shows the effect of crosshatch pattern is an additive term to the final counts from the pixel. This term is a linear function of the slope of the spectrum inside a pixel. As expected, due to symmetry, when the crosshatch is in the middle of the pixel (i.e., $x = \frac{1-w}{2}$), the second term vanishes. Also under the limiting case of QE inside the defect being the same as the outside (i.e., $q_d = q$), or when $w = 0$, the second term vanishes and $C_{\text{s measured flat corrected}} = C_s$.

Typically in spectrographs, the spectrum is spread over a number of pixels in the cross-dispersion direction (width of the slit/fiber). Let N be the number of pixels the spectrum is spread in the cross-dispersion direction. After 2-D to 1-D sum extraction of the spectrum (we assume sum extraction here for ease of explanation, rather than optimal extraction, which is what we use in reality), the total counts in the i'th pixel of the 1-D spectrum will be

$$A(i) = \sum_j^N C_{s_j} + \sum_j^N \frac{Sw(q-q_d)\left[\frac{1-w}{2} - x(j)\right]}{[wq_d + (1-w)q]}, \tag{2}$$

where x and q_d are dependent on j (j is the index of the pixel in cross-dispersion direction).

Let the true spectrum, which we would have obtained if there was no defect in the i'th pixel, be $A_o(i)$. (In practice, we can measure this in a high-resolution spectrograph when the star is at a different barycentric velocity, which moves the spectrum multiple pixels away from the defective pixel.) Then $A_o(i) = \sum_j^N C_{s_j}$. If the spectrograph's cross-dispersion slit profile is top hat shaped like in the case of HPF, we can simplify $C_{s_j} = A_o(i)/N$, and the slope in pixel space $S = \frac{1}{N}\frac{\mathrm{d}A_o}{\mathrm{d}\lambda}\Delta\lambda$, where $\Delta\lambda$ is the wavelength dispersion per pixel. (For a general cross-dispersion profile, one has to keep this summation as it is. However, it does not change the additive nature of the equation nor inferences in the subsequent sections of this paper.)

3.4 *RV Error Introduced by the Crosshatch Pattern*

The fundamental equation to calculate the RV from the change in flux of a spectrum at pixel i is given by the following equation:[6]

$$\frac{\delta V(i)}{v_c} = \frac{A(i) - A_o(i)}{\lambda(i)\left(\frac{\mathrm{d}A_o}{\mathrm{d}\lambda}\right)_i}, \tag{3}$$

where $\delta V(i)$ is the RV shift and v_c is the velocity of light.

Substituting Eq. (2) into Eq. (3), we obtain the expression for the spurious RV induced by the crosshatch:

$$\frac{\delta V(i)}{v_c} = \frac{\Delta\lambda}{\lambda(i)}\frac{1}{N}\sum_j^N \frac{w(q-q_d)\left[\frac{1-w}{2} - x(j)\right]}{[wq_d + (1-w)q]} = \frac{\Delta\lambda}{\lambda(i)}\xi, \tag{4}$$

where

$$\xi = \frac{1}{N}\sum_j^N \frac{w(q-q_d)\left[\frac{1-w}{2} - x(j)\right]}{[wq_d + (1-w)q]}. \tag{5}$$

We note an important feature in the expected RV noise from a single pixel is that this quantity is independent of the slope of the spectrum! For pixels containing crosshatch, $x(j)$ is a straight line whose angle and position can be measured from the flat images as detailed in Sec. 2.

3.5 *RV Impact on HPF*

The q_d inside the crosshatch of HPF's H2RG varies across the detector. A typical value in HPF for q_d/q is 0.54, width $w = 1/3.78$, and the slope of the line defining $x(i)$ is 14.8 deg (see Sec. 2 for more details on these measurements). This 14.8 deg implies a continuous line of subpixel crosshatch defect crosses 3.8 pixel rows while moving from one column pixel to the next. HPF was designed to image the fiber slit across 2.5×9.5 pixels as shown in Fig. 3. To enable this averaging, the rectangular slit was rotated and carefully aligned vertically along the pixel columns. Due to the symmetry of the $(\frac{1-w}{2} - x)$ term in Eq. (4), RV error will cancel out if all the 3.8 pixels affected by a crosshatch defect are fully inside the 9.5-pixel slit image of HPF. However, when the crosshatch pattern appears near the edge pixels of the slit they do not cancel out, resulting in a residual error. By discretising the position of the crosshatch pattern on a 10-pixel slit column, we can approximate HPF's pixel level RV errors to five discrete ξ values. Figure 3(a) shows the probabilistic histogram of these pixel level ξ values for an order

Downloaded From: https://www.spiedigitallibrary.org/journals/Journal-of-Astronomical-Telescopes,-Instruments,-and-Systems on 29 Oct 2019
Terms of Use: https://www.spiedigitallibrary.org/terms-of-use

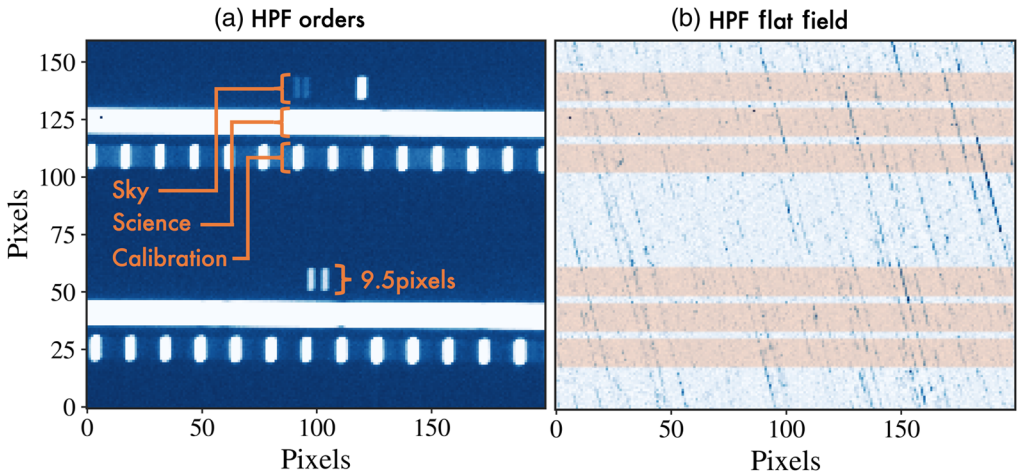

Fig. 3 (a) A zoom in on-sky science image showing only two orders showing the HPF science, sky, and calibration order traces. (b) The same as (a) but during a filtered flat-field exposure to illustrate the size of the crosshatch pattern with order traces overlaid.

where k is the fraction of the column pixels in that order which are affected by crosshatch defects.

The net stellar RV measured by the least-squares technique[7,8] is equivalent to an optimally weighted average of the pixel level RV values given by Eq. (4). The optimal weights are given by Eq. (8) in Ref. 6, which is proportional to $\lambda^2(i)\frac{\mathrm{d}A^2}{\mathrm{d}\lambda}$. Using HPF's dispersion solution, along with the spectrum of a typical M-dwarf star (specifically, Barnard's star), we calculated the optimal weights and thereby the weighed average of pixel level RVs drawn from the probability distribution of ξ shown in Fig. 4(a). Figure 4(b) shows the typical 1 sigma error due to crosshatch defects in the RV estimated for this M-dwarf star from a single order (2040 pixel columns), as a function of k, where k is the fraction of pixels in the order affected by crosshatch defects.

3.6 *Caveats of the Model*

The major caveat to our model is that we are treating the crosshatch pattern originating from crystal defects as pure subpixel low QE regions. We are ignoring all the other possible artifacts in the pixel behavior due to its impact on electron mobility, diffusion, etc. For the sake of simplicity, we are also assuming a step function model with constant width for the subpixel QE difference. We also made the assumption that the spectrum after convolution with instrumental PSF is smooth enough to be locally approximated by a line with slope S inside a pixel. To cancel out the crosshatch effect inside an extended slit like in case of HPF, the q_d should not vary. This is only partially true in certain areas of HPF detector. When q_d varies rapidly at small pixel length scales the noise in RV will be even higher than suggested by Fig. 4(b). The result in Fig. 4(b) is sensitive to the q_d, hence they should be treated only as a typical order of magnitude estimate of the RV error due to the crosshatch defects. The discretization of the ξ for the calculation also makes this result an approximation. In this calculation, we ignored the effects due to correlation in the presence or absence of crosshatch across nearby column pixels. We also ignored the scenario of crosshatch patterns overlapping inside the same pixel. Despite these caveats, this model can be easily extended to any subpixel QE defects of any detector. The RV impact estimate calculated in Sec. 3.5 is specific to HPF due to the slit length used, as well as the constant angle of crosshatch. However, these calculations can be easily modified for any spectrograph with different slit

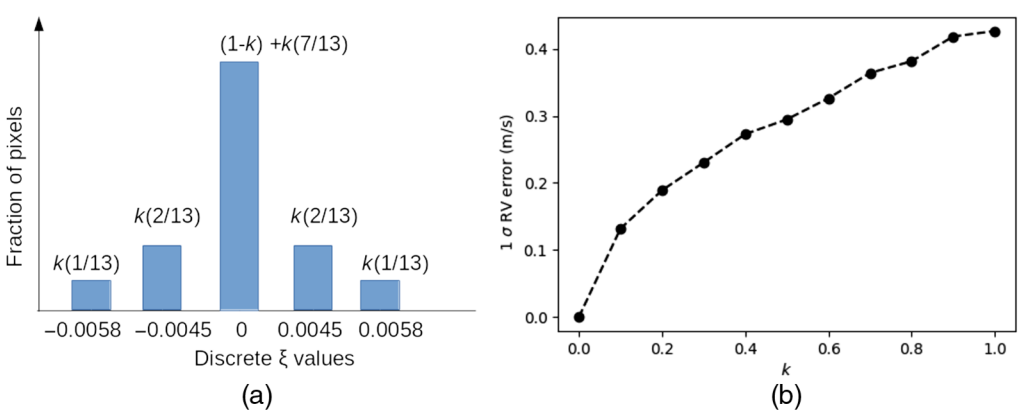

Fig. 4 (a) The probabilistic histogram of pixel level discretised ξ values causing the crosshatch induced RV errors in HPF. k is the fraction of pixels in a spectrum affected by crosshatch defects. (b) 1 sigma RV error as a function of k for a typical mid-M-dwarf star spectrum in a typical order of HPF due to crosshatch pattern.

Downloaded From: https://www.spiedigitallibrary.org/journals/Journal-of-Astronomical-Telescopes,-Instruments,-and-Systems on 29 Oct 2019
Terms of Use: https://www.spiedigitallibrary.org/terms-of-use

lengths. If the detector has multiple crosshatch angles, as long as the fraction of pixels on which multiple crosshatches overlap are small this method can still be used to get an estimate of the impact on RV measurement.

4 Correction Algorithm

The vertical rectangular fiber slit of HPF enables us to reduce the 2-D intrapixel inhomogeneity into a simpler 1-D problem. In this section, we outline the rationale behind the proposed 1-D spectrum correction algorithm for HPF.

The optical cross-dispersion profile of the HPF's trace is locally a well-defined shape since the flux contribution from nearby wavelengths is constant across the rectangular slit profile. (Note that this is not generally true for spectrographs fed by bare, nonsliced, and nonrectangular fiber.) Let us denote this cross-dispersion profile across 10 pixels as a 10-dimensional normalized vector, P. Let f be the scalar quantity that represents the total flux at any given pixel column in the trace. Then the profile at that column in trace is given by the vector fP. Let us denote the effective gain and QE correction (for a flat spectral source) at each 10 pixels inside the profile by the vector G. The sum-extracted 1-D spectrum is then given by the dot product of these vectors $=G \cdot fP = fG \cdot P$. This separability of f and $G \cdot P$ at each column in a trace of HPF due to the rectangular slit is the key aspect of HPF, which enables us to use this 1-D algorithm. For a nonflat spectral source like a star (f_s), based on Eq. (1), we expect an additive term proportional to the slope of the spectrum, i.e., the measured sum-extracted spectrum will be $f_s G \cdot P + c\frac{\mathrm{d}f_s}{\mathrm{d}\lambda}$, where the proportionality constant c encodes all the averaged effective w and q_d values.

To correct for the crosshatch pattern error, we propose the following steps.

Step 1: The first step is to divide the 1-D extracted spectrum using the 1-D extracted spectrum of a normalized flat illumination source. This step removes the $G \cdot P$ term from the flux resulting in the output to be

$$f_s + \frac{c}{G \cdot P}\frac{\mathrm{d}f_s}{\mathrm{d}\lambda}. \tag{6}$$

Step 2: The slope of the spectrum $\frac{\mathrm{d}f_s}{\mathrm{d}\lambda}$ is either calculated iteratively or from a multiepoch average template spectrum, which (due to barycentric/instrumental shift) is not affected by the nondefective pixel.

Step 3: Slope is multiplied with $c/(G \cdot P)$ to obtain the additive correction, which needs to be subtracted out from the extracted spectrum after step 1 [Eq. (6)] to recover f_s. The following section explains how the required coefficient $c/(G \cdot P)$ is calculated for each column pixel in the trace of the spectrum.

4.1 *Calculation of the Correction Coefficient*

For estimating the proportionality constant of the correction term due to the slope of the spectrum [i.e., $c/(G \cdot P)$ in Eq. (6)], we need a spectral source with known spectral slope and flux. By shifting the spectrum in wavelength or frequency, across each column pixel, we can measure the excess flux as a function of the slope. Note that, since we are doing the direct measurement of the correction from the data, many of the caveats of the approximations we made in our theoretical model to understand the problem, described in earlier sections, are irrelevant for our proposed correction algorithm. In theory, a late type star observed under a range of barycentric shift will enable the calibration of at least few regions of the spectrum. For robust estimation of the proportionality coefficient, one needs a spectral source with maximum slope allowed by the optical PSF of the instrument. This calibration could be performed with a tunable LFC as is further discussed below.

4.2 *Using Laser Frequency Comb for Measuring Intrapixel QE*

A subpixel tuneable LFC enables us to scan the sharpest instrumental profile of HPF across a pixel yielding maximum leverage on estimating intrapixel QE variations. The large change in

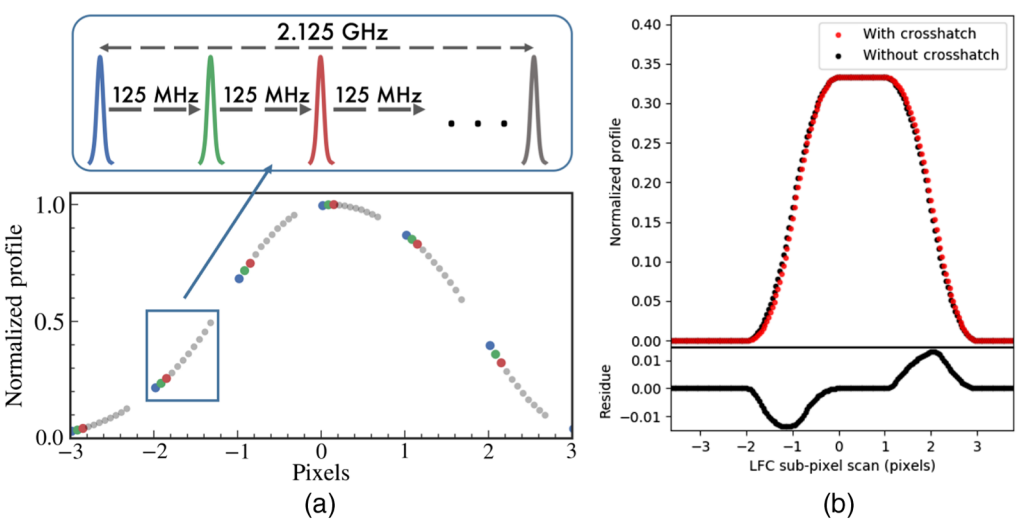

Fig. 5 (a) Current capability of the HPF LFC: experimental results showing the 1-pixel scanning (in 125 MHz steps) of the HPF's PSF. (b) Red curve shows the simulated LFC profile traced by a pixel with intrapixel QE defect, during a full profile scan with the future upgraded LFC. Black curve is the reference curve when all the pixels are free of crosshatch defects.

Downloaded From: https://www.spiedigitallibrary.org/journals/Journal-of-Astronomical-Telescopes,-Instruments,-and-Systems on 29 Oct 2019
Terms of Use: https://www.spiedigitallibrary.org/terms-of-use

slope of the spectrum when an LFC line is swept across a pixel gives a tight estimate of the proportionality coefficient $c/(G \cdot P)$. Note that this coefficient captures in it the effective width and q_d of the subpixel defect, even though our model was a naive step function.

Currently, HPF's LFC[2] enables us to scan only a frequency range corresponding to a 1-pixel width in the HPF focal plane. Figure 5(a) shows the super-resolution trace of the instrumental profile we generated by scanning the current LFC at subpixel positions. After a proposed future upgrade to the HPF LFC, we will be able to scan the LFC by 30 GHz, enabling us to scan all the pixels in the spectrum with subpixel resolution. Figure 5(b) shows a simulation of the normalized profile trace we would obtain for a simulated single pixel with intrapixel QE defect. The difference in the profile to the normal profile of the LFC as a function of slope will directly constrain the correction coefficient.

5 Conclusion

Using a simple toy-model, we have shown that the crosshatch pattern induced correction term is additive and proportional to the slope of the underlying flux illumination on the pixel. Our simple model also enables calculation of the RV impact of these crosshatch patterns. We show that spreading the light across multiple pixels in the cross dispersion helps ameliorate the impact of these defects, which we estimate to be $\sim$0.4 m/s for HPF (with stated caveats, including the assumption that most or all of the pixels in the order suffer from crosshatch issues) for RVs from a single order of a typical mid M-star. In reality, for the actual HPF detector, the location of the red halves of the red-most echelle orders is significantly more affected by this issue ($k \sim 1$) than the location of the blue halves of the blue-most echelle orders ($k \sim 0.1$). Future work will model the actual HPF detector. We also present a technique to determine the typical characteristics of these subpixel crosshatch patterns from flat images. We find that for HPF's detector the typical width of the crosshatch pattern is $\sim$5 μm, and the QE inside the defect relative to outside is $\sim$54%. The QE varies significantly across the defects, and the density of the crosshatches also varies significantly across the detector. Modern NIR detectors still remain as a major source of systematic error in precision NIR RVs. While better detectors are always the solution, we also demonstrate a proof-of-concept experiment to enable characterization of these defects employing a tunable frequency-stabilized laser comb (LFC).

Acknowledgments

Authors thank organizers of ISPA-2018 for organizing a very informative and interactive workshop. This work was partially supported by the funding from the Center for Exoplanet and Habitable Worlds. The Center for Exoplanet and Habitable Worlds is supported by Pennsylvania State University, Eberly College of Science, and Pennsylvania Space Grant Consortium. We acknowledge support from NSF Grant Nos. AST1006676, AST1126413, AST1310885, and AST 1310875; and the NASA Astrobiology Institute (No. NNA09DA76A) in our pursuit of precision radial velocities in NIR, and support from the Heising-Simons Foundation. Computations for this research were performed on Pennsylvania State University's Institute for Cyber-Science Advanced CyberInfrastructure (ICS-ACI). We thank the HET staff for their critical assistance, expertise and support. Data presented herein were obtained at the Hobby-Eberly Telescope (HET), a joint project of the University of Texas at Austin, Pennsylvania State University, Ludwig-Maximilians-Universität München, and Georg-August Universität Gottingen. The HET is named in honor of its principal benefactors, William P. Hobby and Robert E. Eberly. The HET collaboration acknowledges the support and resources from the Texas Advanced Computing Center. Software: astropy,[9] numpy,[10] scipy,[11] matplotlib,[12] CoCalc,[13] Sympy.[14] *Disclosures*: The authors declare that there are no known conflicts of interest. The mention of specific companies and trade names is for scientific and technical purposes only and does not constitute an endorsement by NIST.

References

1. S. Mahadevan et al., "The Habitable-Zone Planet Finder: a status update on the development of a stabilized fiber-fed near-infrared spectrograph for the for the Hobby–Eberly telescope," *Proc. SPIE* **9147**, 91471G (2014).
2. A. J. Metcalf et al., "Stellar spectroscopy in the near-infrared with a laser frequency comb," *Optica* **6**, 233–239 (2019).
3. T. Hardy et al., "Intra-pixel response of infrared detector arrays for JWST," *Proc. SPIE* **7021**, 70212B (2008).
4. C. Shapiro, E. Huff, and R. Smith, "Intra-pixel response characterization of a HgCdTe near infrared detector with a pronounced crosshatch pattern," *Proc. SPIE* **10709**, 1070936 (2018).
5. P.-E. Crouzet et al., "Euclid H2RG detectors: impact of crosshatch patterns on photometric and centroid errors," *Proc. SPIE* **10709**, 107090Q (2018).
6. F. Bouchy, F. Pepe, and D. Queloz, "Fundamental photon noise limit to radial velocity measurements," *Astron. Astrophys.* **374**, 733–739 (2001).
7. G. Anglada-Escudé and R. P. Butler, "The HARPS-TERRA project. I. Description of the algorithms, performance, and new measurements on a few remarkable stars observed by HARPS," *Astrophys. J. Suppl. Ser.* **200**, 15 (2012).
8. M. Zechmeister et al., "Spectrum radial velocity analyser (SERVAL). High-precision radial velocities and two alternative spectral indicators," *Astron. Astrophys.* **609**, A12 (2018).
9. A. M. Price-Whelan et al., "The astropy project: building an open-science project and status of the v2.0 Core package," *Astron. J.* **156**, 123 (2018).
10. S. van der Walt, S. C. Colbert, and G. Varoquaux, "The numpy array: a structure for efficient numerical computation," *Comput. Sci. Eng.* **13**, 22–30 (2011).
11. E. Jones et al., "SciPy: open source scientific tools for Python," 2001, http://www.scipy.org/ (18 October 2019).
12. J. D. Hunter, "Matplotlib: a 2-D graphics environment," *Comput. Sci. Eng.* **9**, 90–95 (2007).
13. I. SageMath, "CoCalc collaborative computation online," 2019, https://cocalc.com/.
14. A. Meurer et al., "SymPy: symbolic computing in python," *PeerJ Comput. Sci.* **3**, e103 (2017).

Joe P. Ninan received his PhD from the Tata Institute of Fundamental Research, Mumbai, in 2016. He is a CHEW postdoctoral fellow at Pennsylvania State University. He works on young stellar objects, and calibration and algorithm development for various optical and near-infrared instruments. He is a member of the instrument team developing the NEID and Habitable-Zone Planet Finder (HPF) Doppler spectrometers.

Suvrath Mahadevan received his PhD from the University of Florida in 2006. He is an associate professor at Pennsylvania State University. His interests include precision spectroscopy and photometry, M dwarfs, large-scale spectroscopic surveys, astronomical instrumentation, astrophotonics, and astrobiology. He is the principal investigator for the NEID and HPF Doppler spectrometers.

Gudmundur Stefansson is a NASA Earth and space science fellow and PhD candidate in astronomy and astrophysics at Pennsylvania State University, where his thesis research focuses on developing

Downloaded From: https://www.spiedigitallibrary.org/journals/Journal-of-Astronomical-Telescopes,-Instruments,-and-Systems on 29 Oct 2019
Terms of Use: https://www.spiedigitallibrary.org/terms-of-use

next-generation instrumentation and techniques to detect and precisely characterize exoplanets.

Chad Bender received his PhD from Stony Brook University in 2006. He is an associate astronomer at the University of Arizona's Steward Observatory. His research focuses on characterizing the orbital dynamics and atmospheric structures of faint binary companions, and ranging in mass from stars to Earth-sized exoplanets. He is the instrument scientist for the HPF and NEID Doppler spectrometers.

Arpita Roy received her PhD from Pennsylvania State University in 2017. She is a Robert A. Millikan prize postdoctoral fellow at California Institute of Technology working on exoplanet discovery and characterization using the new wave of extreme precision spectroscopy instruments. She is a project scientist for the Keck Planet Finder instrument, and a member of the HPF and NEID instrument teams, spanning both the optical and near-infrared in search of Earth-like planets.

Kyle F. Kaplan received his PhD in astronomy from the University of Texas at Austin in 2017. He is a postdoctoral research associate at the University of Arizona's Steward Observatory. He is a member of the HPF and NEID instrument teams and works on developing and implementing the data reduction pipeline software for both instruments. His research focuses on high-resolution spectroscopic observations of photodissociation regions, planetary nebulae, and emission from Earth's atmosphere.

Connor Fredrick is a PhD candidate in physics at the University of Colorado Boulder and National Institute of Standards and Technology (NIST). His thesis research focuses on developing techniques and technologies related to lasers, nonlinear optics, and optical frequency combs (OFC) for application in precision astronomical spectroscopy. He is a member of the OFC design team for the HPF Doppler spectrometer.

Andrew J. Metcalf received his PhD from Purdue University in 2015 and was a postdoc at NIST from 2015 to 2018. He is a research scientist at the Air Force Research Laboratory's Space Vehicles Directorate. He is a member of the OFC design team for the HPF Doppler spectrometer.

Andrew Monson received his PhD from the University of Wyoming in 2009. He is an assistant research professor at Pennsylvania State University. He works on developing and commissioning astronomical instrumentation. He is the systems engineer for the HPF and NEID spectrographs. Prior to Penn State, he worked at Carnegie Observatories to develop and commission FourStar, a wide field near-infrared imager.

Ryan Terrien received his PhD from Pennsylvania State University in 2015 and was a National Research Council postdoctoral researcher at NIST, Boulder, Colorado, USA from 2016 to 2017. He is an assistant professor of physics and astronomy at Carleton College. He is a core member of the HPF and NEID instrument and science teams.

Lawrence W. Ramsey received his PhD from Indiana University, Bloomington, Indiana, in 1976. He is a professor of astronomy and astrophysics and Eberly College of Science Distinguished Senior Scholar Emeritus at Pennsylvania State University. He has been at Penn State since 1976, where he pursued research in stellar activity, stellar seismology, astronomical instrumentation, and exoplanet searches. A major focus since 1990 has been implementing the Hobby–Eberly telescope, the concept for which he and Penn State colleagues developed in 1983.

Scott A. Diddams received his PhD from the University of New Mexico in 1996. He is a fellow of NIST and an adjoint professor at the University of Colorado. From 1996 through 2000, he did postdoctoral work at JILA in Boulder, Colorado, USA. His research interests include ultrafast nonlinear optics, as well as the development of laser frequency combs for optical clocks, metrology, spectroscopy, and astronomy.

Downloaded From: https://www.spiedigitallibrary.org/journals/Journal-of-Astronomical-Telescopes,-Instruments,-and-Systems on 29 Oct 2019
Terms of Use: https://www.spiedigitallibrary.org/terms-of-use